nature materials

Article

https://doi.org/10.1038/s41563-026-02604-8

Boosting ionic conductivity of single-ion conductive polyelectrolyte elastomers via high-dielectric plasticizers

Received: 17 July 2025

Accepted: 12 April 2026

Published online: 03 June 2026

Check for updates

Sangjun Ma[1], Solji Ahn[1], Jae-Man Park[1], Hakjun Lee[1], Seong-Yu Choi[1], Yong Eun Cho[1], Dong-yup Lee[1], Seung-Woo Lee[1], Maga Kim[1], Seung Won Moon[1], Yun Hyeok Lee[1], Yong-Woo Kim[1], Tae-Woo Lee[1,2,3,4] & Jeong-Yun Sun[1,2]

Ionic conduction plays a vital role in biological systems, energy storage and ionotronic devices. Polyelectrolyte elastomers have attracted growing interest as solid-state single-ion conductors due to their inherent ion selectivity, leakage-free nature and mechanical elasticity. However, existing polyelectrolyte elastomers have relatively low ionic conductivity (~10^{-3} mS cm^{-1}), limiting their applicability as efficient ionic conductors. Here we present a materials design approach that boosts conductivity and preserves leakage-free operation by introducing a solid-state additive that combines two key characteristics: a high dielectric constant to increase dissociated ion density (n) and a plasticizing effect to enhance ion mobility (μ). Demonstrated with succinonitrile, this approach increases conductivity by over two orders of magnitude at room temperature across both polycationic and polyanionic systems, further enhancing elasticity. By elevating conductivity across diverse polyelectrolyte networks, this work demonstrates a versatile route to achieve stable and efficient ion transport for next-generation solid-state single-ion conductors.

Ionic conduction plays a central role in both natural and artificial systems. In biological contexts, it governs phenomena such as neural signalling[1] and sensory processing[2]. In engineered platforms, it enables a wide range of electrochemical technologies, including energy storage devices[3], organic electrochemical transistors[4] and ionotronic systems such as soft actuators[5], sensors[6] and logic circuits[7,8]. Among various ionic conductors, polymer electrolytes such as hydrogels with dissolved salts[9] or ionogels[10] have attracted considerable attention due to their mechanical softness, transparency and processability.

Despite their high conductivity, the free movement of both cations and anions makes these systems less ideal for applications[11] that require the selective transport of a single ionic species, such as ionic thermoelectric devices[12,13], ionic diodes[7,14] and osmotic energy conversions[15]. Polyelectrolyte gels, which incorporate fixed charged groups along the polymer backbone, enable single-ion conduction and maintain relatively high ionic conductivity. However, their reliance on liquid components introduces issues such as leakage and evaporation, which compromise operational stability under ambient conditions[16].

Polyelectrolyte elastomers (PEs), an emerging class of solid-state ionic conductors, address the stability issues associated with liquid-containing gels[7,8,17–19]. By covalently tethering one bulky ionic species to a crosslinked polymer network, PEs exhibit a low glass transition temperature (T_g), allowing the mobile counterions to diffuse in the dry state and maintain mechanical elasticity[20]. Despite these advantages,

[1]Department of Materials Science and Engineering, Seoul National University, Seoul, Republic of Korea. [2]Research Institute of Advanced Materials (RIAM), Seoul National University, Seoul, Republic of Korea. [3]Interdisciplinary Program in Bioengineering, Institute of Engineering Research, Soft Foundry, Seoul National University, Seoul, Republic of Korea. [4]SN Display Co. Ltd, Seoul, Republic of Korea. e-mail: jysun@snu.ac.kr

PEs exhibit low ionic conductivity in the range of 10^{-4}–10^{-2} mS cm^{-1}, limiting their applicability in systems demanding fast or efficient ion transport. A practical target is, therefore, to narrow this conductivity gap by approaching the level of ~1 mS cm^{-1} (ref. 21), commonly reached by liquid-based ionic conductors at room temperature[22].

Many studies have attempted to address the long-standing challenge of low ionic conductivity in PEs. As the ionic conductivity (σ) in solid-state PEs is determined by the product of dissociated ion density (n) and their mobility (μ) (Fig. 1a,b), previous approaches can be broadly categorized into two types: one aims to increase n by introducing functional groups[17,23] or engineering structural motifs[24] to enhance ion dissociation, whereas the other focuses on improving μ by lowering the polymer T_g through copolymerization with flexible segments[18,25–27]. Nonetheless, these strategies typically showed conductivities below ~10^{-1} mS cm^{-1} at room temperature. To further increase conductivity, liquid plasticizers are often incorporated into single-ion electrolyte systems[28], but such approaches introduce issues of evaporation or leakage. We, therefore, hypothesized that simultaneously enhancing both n and μ using a solid-state additive, rather than a liquid component, would provide a more effective pathway to achieve high ionic conductivity in solid-state PEs and retain their inherent leakage-free stability (Fig. 1c).

Here we report leakage-free highly conductive polyelectrolyte elastomers (HCPEs) enabled by incorporating a high-dielectric plasticizer. Succinonitrile (SN), a solid-state plasticizer with a strong dipolar character[29], showed the simultaneous enhancement of segmental mobility and ion dissociation when incorporated into PEs. This approach was applicable to both polycationic and polyanionic systems, achieving conductivities of up to 0.78 and 1.57 mS cm^{-1} at room temperature, which are 318 and 103 times higher than their pristine states, respectively. The HCPEs maintained their solid-state form and elastomeric behaviours without the leakage of SN. Leveraging their high ionic conductivity, mechanical elasticity and leakage-free stability, the HCPEs were further demonstrated as capacitive sensors with broad-range pressure detection. Moreover, this approach extends to diverse solid-state single-ion network polymers with different polymer backbones and mobile counterions, substantially increasing their ionic conductivity.

Design principles of increasing ionic conductivity

To construct single-ion-conducting PEs, we synthesized polycationic and polyanionic acrylate monomers, following previously reported procedures[7,17] (Supplementary Methods and Supplementary Figs. 1 and 2). Although PEs exhibit intrinsic ion selectivity, their ionic conductivity is fundamentally limited by two factors: low dissociated ion density and restricted ion mobility.

To increase n, we focused on weakening the electrostatic interactions between ionic charges by increasing the dielectric constant of the medium, which has also been suggested to favour ion transport under weaker electrostatics[24,30]. The electrostatic interaction can be described by Coulomb's law:

$$E_c = \frac{q_+ q_-}{4\pi\varepsilon_0\varepsilon_s r}, \quad (1)$$

where q_+ and q_- are positive and negative ionic charges, respectively; ε_0 is the vacuum permittivity; ε_s is the static dielectric constant of the medium; and r is the distance between ionic charges. In our elastomer systems, all ions are monovalent, so $q_\pm = e$, where e is the elementary charge. Therefore, increasing the dielectric constant of the polymer matrix reduces Coulombic energy, facilitating ion dissociation[31]. In addition, the incorporation of additives with affinity for ionic species may increase r, further reducing electrostatic binding. However, enhancing ionic conductivity requires more than dielectric screening alone. For high conductivity, dissociated counterions also move efficiently through the polymer matrix. In solvent-free systems, ion mobility is known to depend on the segmental motion of polymer chains[32]. Therefore, an ideal additive compatible with PEs not only raises the dielectric constant to promote ion dissociation but also acts as a plasticizer to increase polymer chain mobility. At the same time, to maintain the intrinsic advantages of PEs, such as ion selectivity and leakage-free properties, the additive should be an electrically neutral solid that does not introduce additional mobile ions or form a liquid phase prone to leakage.

Guided by these design principles, we selected SN as the high-dielectric plasticizer. SN exhibits a relatively high dielectric constant[29] (Supplementary Fig. 3a) and acts as an effective plasticizer[33]. It also possesses a wide electrochemical window[29], supporting its electrochemical stability in ion-conducting systems. Furthermore, SN is non-ionic and remains solid at room temperature (Supplementary Fig. 3b–d), which preserves the inherent ion-selective and leakage-free properties of PEs.

SN was introduced into as-prepared PEs by a facile post-treatment process (Supplementary Fig. 4), and the loading range was limited to avoid phase separation (Supplementary Fig. 5). On the basis of the precipitation threshold, we defined a series of HCPE compositions: SN 0.2, SN 0.4 and SN 0.6 for polycation; and SN 0.3, SN 0.6 and SN 0.9 for polyanion. The numerical label represents the weight ratio of SN relative to the dry elastomer matrix. The resulting HCPEs remained transparent, indicating a uniform distribution of SN (Supplementary Fig. 6a). Raman mapping, X-ray diffraction and differential scanning calorimetry further showed that SN was uniformly dispersed in the network without forming a separate crystalline phase (Supplementary Figs. 6–8). Attenuated total reflection (ATR) Fourier transform infrared (FTIR) confirmed the successful incorporation of SN and the absence of dichloromethane (DCM), validating the solvent-free nature of the final elastomers (Supplementary Fig. 9).

To experimentally examine these design principles, we compared four additives with distinct dielectric constants and plasticizing abilities: dimethyl carbonate (DMC; $\varepsilon_s \approx 3$)[34], a zwitterionic liquid (ZIL; $\varepsilon_s \approx 285$) (Supplementary Fig. 10), polyethylene glycol 200 (PEG 200; $\varepsilon_s \approx 18$)[35] and SN ($\varepsilon_s \approx 55$) (Fig. 1d). These additives were incorporated into the PEs, and impedance-based spectroscopy was used to decouple the effects on dissociated ion density (n) and effective ion mobility (μ) (Supplementary Note 1, Supplementary Figs. 11 and 12 and Supplementary Table 1). DMC, a low-dielectric plasticizer, showed negligible changes in conductivity or ion dissociation, with only a slight increase in mobility. ZIL enhanced ion dissociation due to its high polarity, but failed to improve mobility and even reduced it, resulting in limited conductivity gain. PEG 200 increased both parameters moderately and, thus, showed improved conductivity. Among these, SN led to the most pronounced increases in both n and μ, resulting in the highest conductivity among all additives. These results demonstrate that effective conductivity enhancement in solid-state polyelectrolytes cannot be achieved by improving either dielectric screening or polymer plasticization solely; rather, both must be simultaneously considered. Within this framework, SN-containing HCPEs achieve conductivities of 0.78 and 1.57 mS cm^{-1} at room temperature in polycationic and polyanionic systems, respectively. These conductivities are about one order of magnitude higher than the highest values previously reported for solid-state single-ion conductors (Supplementary Fig. 13). In particular, despite their solid-state single-ion nature, their conductivities approach those of dual-ionic conductors such as neat ionic liquids, ionogels and ionic elastomers (Supplementary Table 2). To further elucidate the pronounced conductivity enhancement by SN, we next examined how variation in SN content influences the ionic transport behaviour of HCPEs.

Enhancing ion dissociation by high-dielectric property

To quantify the dielectric environment of the polyelectrolyte matrix, we measured the frequency-dependent permittivity of both polycation

https://doi.org/10.1038/s41563-026-02604-8

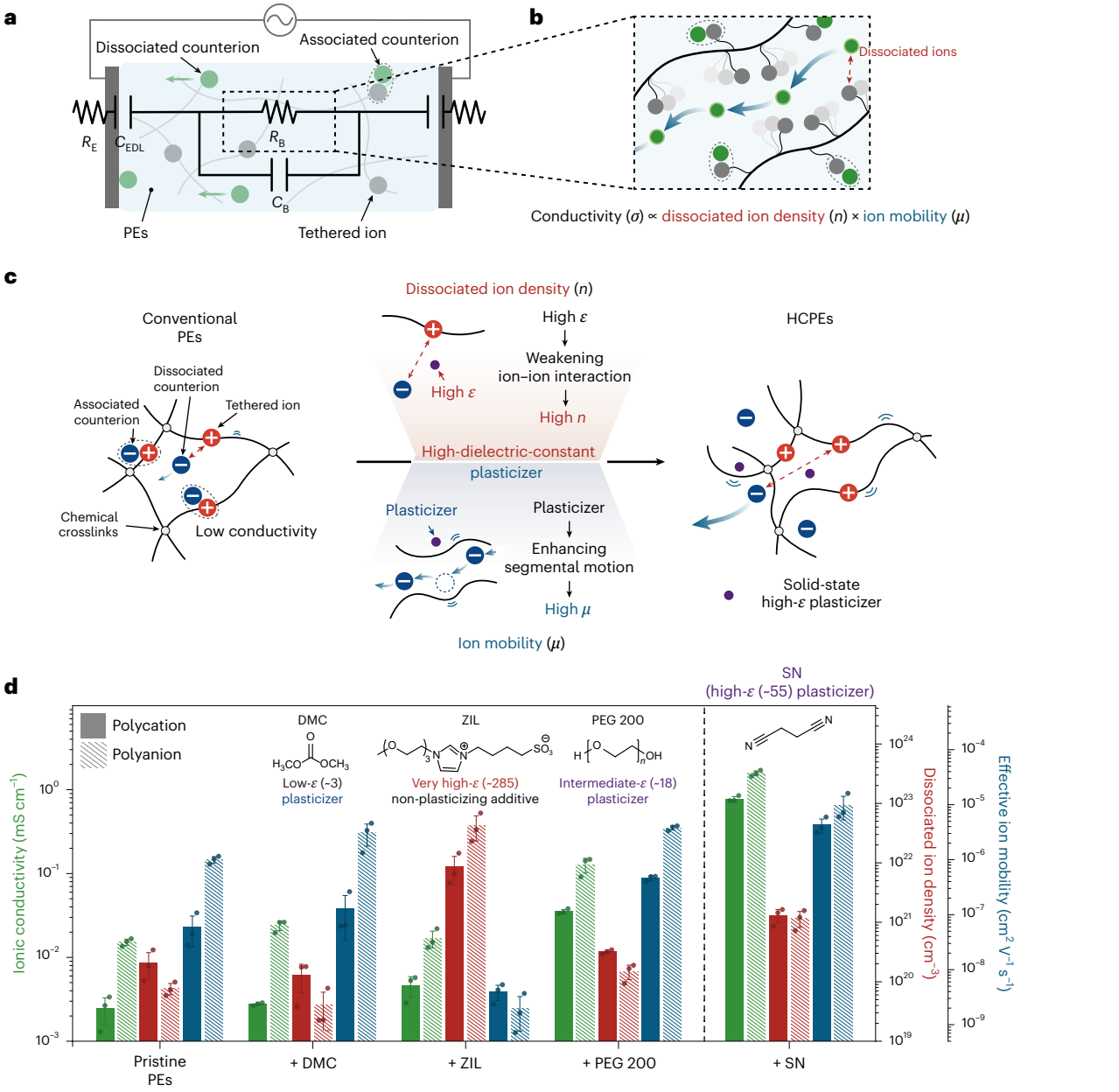

Fig. 1 | Design principle for HCPEs. a, Schematic of an equivalent circuit and ion transport in PEs. PEs consist of tethered ions and mobile counterions, which exist in either dissociated or associated states. Only dissociated counterions contribute to ionic conductivity. The system includes bulk resistance (R_B), electrode resistance (R_E), and capacitive components such as bulk capacitance (C_B) and electrical double-layer capacitance (C_{EDL}). **b**, Conceptual relationship between σ, n and μ, where $\sigma \propto n \times \mu$. Charge transport occurs via migration of dissociated counterions through the polymer matrix, and R_B reflects the resistance associated with this migration process. **c**, Schematic of the design strategy to enhance ionic conductivity in PEs. An effective solid-state additive should exhibit both high dielectric constant to promote ion dissociation and plasticizing characteristics to enhance ion mobility. **d**, Comparison of ionic conductivity, dissociated ion density and effective ion mobility for polycationic (solid bars) and polyanionic (hatched bars) elastomers. Pristine PEs and those containing various additives are shown: a low-dielectric plasticizer (DMC), a very high-dielectric non-plasticizing additive (ZIL), an intermediate-dielectric plasticizer (PEG 200) and a high-dielectric plasticizer (SN). Data are presented as mean values ± standard deviation from three independent replicates.

and polyanion. The dielectric constant increased with SN content in both polycation and polyanion systems (Supplementary Fig. 14), confirming that SN enhances the polarizability of the matrix. On the basis of the elevated dielectric constant, SN incorporation attenuates electrostatic interactions between tethered ions and mobile counterions, thereby facilitating ion dissociation (Fig. 2a and Supplementary Fig. 15).

This screening effect was investigated by analysing the mobile counterions using ATR-FTIR, Raman and nuclear magnetic resonance (NMR) spectroscopy. In polycation systems, the bis(trifluoromethanesulfonyl)imide anion ([TFSI]$^-$) exhibited characteristic blueshifts with increasing SN content: the SO_2 asymmetric stretching band[36,37] shifted from 1,346.7 to 1,349.5 cm^{-1}, CF_3 asymmetric stretching[36] from 1,176.7 to 1,183.9 cm^{-1}, SO_2 symmetric stretching[36] from 1,131.3 to 1,134.3 cm^{-1}, and S–N–S asymmetric stretching[36] from 1,050.7 to 1,055.3 cm^{-1} (Fig. 2b). These consistent blueshifts indicate progressive weakening of the Coulombic association between [TFSI]$^-$ and the fixed imidazolium cation[6,37,38]. The ^{19}F NMR spectra of [TFSI]$^-$ in the polycationic monomer showed a gradual downfield shift with increasing SN content, supporting the weakening of electrostatic interaction between the ions[39] (Fig. 2c). Similarly, in the

https://doi.org/10.1038/s41563-026-02604-8

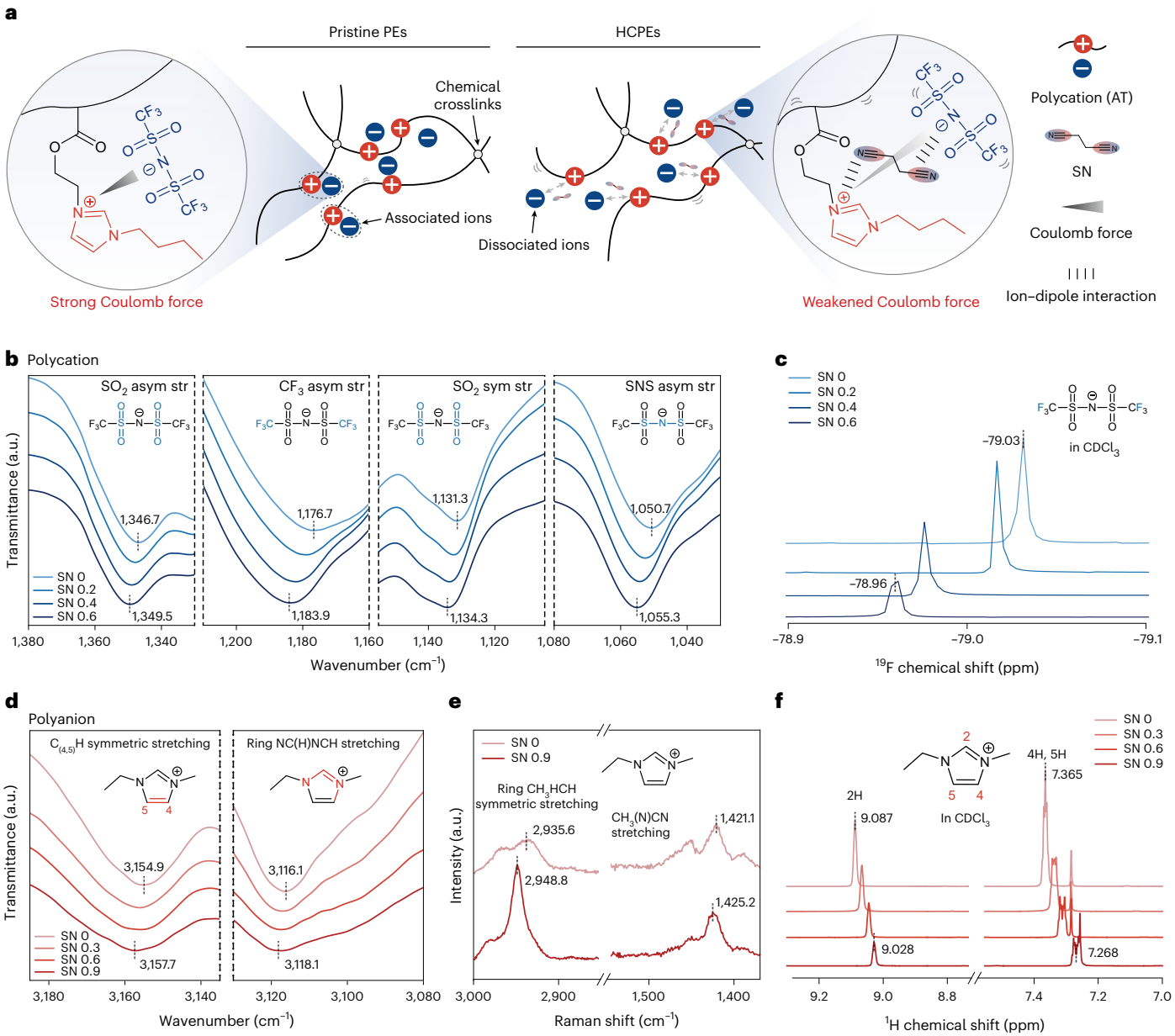

Fig. 2 | Molecular interactions between ions in HCPEs. a, Schematic of the effect of SN incorporation on Coulombic interactions in polycation-based systems. SN reduces the Coulomb force between ions, promoting ion dissociation in HCPEs. **b**, ATR-FTIR spectra of mobile anions in polycations with various SN concentrations. Peak shifts are observed for SO_2 asymmetric stretching (SO_2 asym str), CF_3 asymmetric stretching (CF_3 asym str), SO_2 symmetric stretching (SO_2 sym str) and SNS asymmetric stretching (SNS asym str). **c**, ^{19}F NMR spectra of mobile anions in a polycationic monomer with various SN concentrations. **d**, ATR-FTIR spectra of mobile cations in polyanions with various SN concentrations. Peak shifts correspond to $C_{(4,5)}H$ symmetric stretching and ring NC(H)NCH stretching. **e**, Raman spectra of mobile cations in polyanions (SN 0 and SN 0.9). Peak shifts are observed for ring CH_3HCH symmetric stretching and $CH_3(N)CN$ stretching. **f**, ^1H NMR spectra of mobile cations in polyanionic monomer with various SN concentrations.

polyanion system, the FTIR spectra of 1-ethyl-3-methylimidazolium cation ($[EMIM]^+$) revealed similar shifts: the $C_{(4,5)}H$ symmetric stretching band[37] moved from 3,154.9 to 3,157.7 cm^{-1} and the ring NC(H)NCH stretching band[37] shifted from 3,116.1 to 3,118.1 cm^{-1} (Fig. 2d). Raman vibrational modes for ring CH_3HCH symmetric stretching[36] and $CH_3(N)CN$ stretching[36,40] also shifted from 2,935.6 to 2,948.8 cm^{-1} and from 1,421.1 to 1,425.2 cm^{-1}, respectively, supporting weakened electrostatic interaction between tethered ions and mobile counterions (Fig. 2e). The ^1H NMR spectra also exhibited upfield shifts in the C_2–H, C_4–H and C_5–H peaks of $[EMIM]^+$, consistent with weakened hydrogen bonding and electrostatic association between ions[39] (Fig. 2f). Therefore, these results confirm that SN incorporation weakens Coulombic interactions by enhancing the matrix dielectric constant, thereby promoting ion dissociation.

Plasticization effect on ionic transport properties of HCPEs

In solvent-free, chemically crosslinked polymer networks, long-range polymer chain motion is restricted. In such cases, mobile counterions migrate predominantly via segmental-motion-assisted hopping between neighbouring coordination sites[41]. Therefore, ionic mobility becomes decoupled from the macroscopic viscosity of the electrolyte and instead becomes dependent on the segmental motion of polymer chains[32].

https://doi.org/10.1038/s41563-026-02604-8

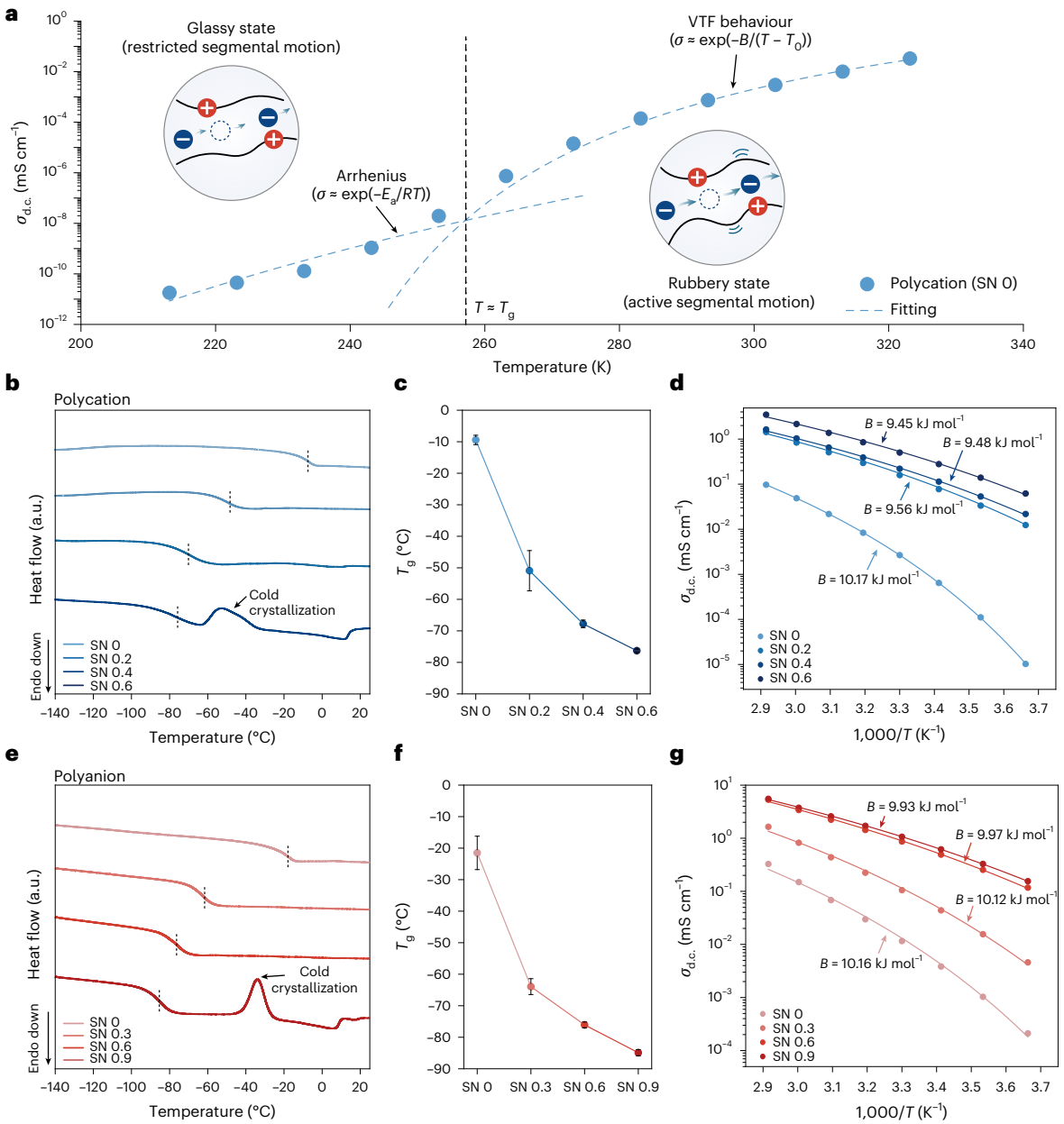

Fig. 3 | Plasticizing characteristics to enhance ion mobility. a, Temperature-dependent $\sigma_{d.c.}$ of polycationic elastomers. Below the glass transition temperature ($T < T_g$, glassy state), restricted segmental motion limits counterion mobility and $\sigma_{d.c.}(T)$ follows Arrhenius behaviour. Above T_g ($T > T_g$, rubbery state), activated segmental motion enhances ion mobility, and $\sigma_{d.c.}(T)$ follows the VTF behaviour. The Arrhenius-to-VTF crossover at $T \approx T_g$ confirms that ion transport is coupled to the polymer's segmental motion. **b**–**d**, Characteristics of polycationic elastomers. **e**–**g**, Characteristics of polyanionic elastomers. **b**,**e**, Thermograms from differential scanning calorimetry are presented. **c**,**f**, T_g as a function of SN content. SN incorporation effectively decreases the polymer's T_g. Data are presented as mean values ± standard deviation from three independent replicates. **d**,**g**, VTF plots of ionic conductivity with various SN concentrations. *B* represents the pseudo-activation energy; solid lines indicate VTF fitting.

In the glassy state ($T < T_g$), the polymer's segmental motion is restricted, leading to a decoupling between ionic motion and polymer dynamics. In this regime, ion transport follows the Arrhenius behaviour, characterized by a temperature-independent activation energy[21]. In the rubbery state ($T > T_g$), increased segmental motion reduces the local friction experienced by ions, thereby promoting higher ionic mobility. In this regime, ion transport follows the Vogel–Tammann–Fulcher (VTF) relation[3,21], confirming that ion transport is facilitated by segmental motion[42]. This temperature-dependent crossover from Arrhenius to VTF behaviour typically occurs near T_g (Fig. 3a and Supplementary Fig. 16). We, therefore, considered that enhancing the polymer segmental motion would lead to improved ion mobility.

To evaluate the plasticizing effect of SN, we measured the differential scanning calorimetry of PEs with varying SN concentrations (Fig. 3b,e). As the SN content increased, T_g gradually decreased, indicating enhanced segmental motion due to plasticization (Fig. 3c,f). We further investigated the temperature-dependent impedance spectra of HCPEs (Supplementary Figs. 17 and 18). At each temperature, the direct current ionic conductivity ($\sigma_{d.c.}$) was calculated. In our HCPEs, the conductivity followed the VTF relation, and the pseudo-activation energy (*B* parameter), which reflects the energetic barrier for ion transport[3], progressively decreased with increasing SN content (Fig. 3d,g and Supplementary Table 3). These results suggest that SN acts as an effective plasticizer and thereby improves ion mobility.

Electrical characteristics and stability of HCPEs

The ionic transport properties of HCPEs were evaluated using electrochemical impedance spectroscopy analysis. As the SN content increased, both polycationic and polyanionic systems exhibited a progressive decrease in complex impedance ($|Z|$), indicating reduced bulk resistance (Fig. 4a,d). The d.c. ionic conductivity increased with the SN content, reaching 0.78 mS cm^{-1} for polycation and 1.57 mS cm^{-1} for polyanion (Fig. 4b,e). These values were obtained by fitting the real part of the conductivity spectra and were further validated by comparing them with conductivities from Nyquist-plot fitting (Supplementary Fig. 19 and Supplementary Table 4). Both systems exhibited a sharp conductivity increase at low SN ratios, followed by gradual saturation, indicating that SN incorporation boosts ionic conductivity in PEs. To understand the origin of conductivity enhancement, we revisited the fundamental relation $\sigma = n\mu e$ and independently quantified n and μ through impedance-based analysis[43–46] (Supplementary Note 1 and Supplementary Table 1). The results show that both n and μ gradually increased with SN content in both polycation and polyanion (Fig. 4b,e). These findings highlight the importance of simultaneously enhancing both parameters to achieve substantial conductivity improvements in solvent-free PEs. We further validated n by independently estimating it from the ATR-FTIR spectra via peak deconvolution[47,48], which yielded values in good agreement with those obtained from electrochemical impedance spectroscopy (Fig. 4c,f, Supplementary Figs. 20 and 21 and Extended Data Table 1). Despite the enhanced conductivity, the master curve of HCPEs' conductivity remained unchanged, suggesting that the conduction mechanism is preserved (Supplementary Fig. 22)[42,49].

To separate the thermodynamic and kinetic contributions to conductivity enhancement, we analysed the temperature dependence of $\sigma_{d.c.}(T)$ by decoupling it into $n(T)$ and $\mu(T)$ (Supplementary Note 3). Similar to the segmental dynamics, the dielectric properties are also temperature dependent (Supplementary Fig. 23); therefore, $n(T)$ and $\mu(T)$ were quantified over the same temperature range. Across both polycationic and polyanionic elastomers, $n(T)$ follows an Arrhenius relation, whereas $\mu(T)$ follows a VTF relation (Extended Data Fig. 1 and Supplementary Table 5), consistent with previous studies[50,51]. These results indicate that the conductivity enhancement arises from increased ion dissociation and enhanced mobility of the dissociated counterions.

To further investigate whether SN facilitates ionic response to the external electric field, we analysed the charge relaxation frequency (τ_C^{-1}) and loss tangent spectra. A shift in τ_C^{-1} towards higher values indicates that ions respond more rapidly to the applied alternating current (a.c.) field[52] (Supplementary Note 2 and Supplementary Figs. 24–26). Consistently, the loss tangent spectrum also shifted to higher frequencies, indicating that the optimal frequency range for the resistive behaviour of ionic conductors moved towards shorter timescales[37] (Supplementary Fig. 27). The improved ionic transport in HCPEs enabled stable electrical operation across a wide frequency range and outperformed previously reported PEs in both conductivity and charge relaxation frequency (Fig. 4g and Supplementary Table 2). To demonstrate this, a simple light-emitting diode (LED) circuit was constructed using polycationic samples at 1-MHz frequency. Although pristine PEs emitted no light, SN-containing HCPEs sustained bright emission (Fig. 4g, inset). These results indicate that our HCPEs combine high conductivity with fast ion response, offering potential for high-frequency ionic applications.

The long-term stability of HCPEs was assessed by monitoring conductivity and weight over 96 h under ambient conditions (25 °C, 35% relative humidity (RH)). Both SN 0.6 (polycation) and SN 0.9 (polyanion) samples exhibited negligible changes in either parameter, confirming their stability in open-air conditions (Fig. 4h and Supplementary Fig. 28). Moisture and water resistance were further evaluated through high-humidity exposure and water contact angle measurements. Under 90% RH conditions, both systems showed minimal mass change, which was lower than PEG 200-based controls (Fig. 4h (inset) and Supplementary Fig. 29). Polycationic samples maintained high hydrophobicity (water contact angle, >100°) regardless of the SN content, whereas polyanionic samples exhibited moderately lower contact angles (70°–75°) (Fig. 4i,j). This behaviour arises from their structural differences, as polycationic networks contain a higher fraction of fluorinated components than polyanionic networks. Therefore, these results confirm that SN incorporation does not compromise environmental stability.

Leakage behaviour under thermal and mechanical stress was also investigated. Samples were placed on commercial oil paper and heated at 60 °C, which is above the melting point of SN for 1 h (Supplementary Fig. 30a). To compare the wetting behaviour of SN and PEG 200 on oil paper, we measured the contact angles of molten SN and PEG 200 on the same oil paper at 60 °C. Both liquids exhibited similar contact angles, indicating comparable wetting on the commercial oil paper (Supplementary Fig. 31). Although PEG 200-containing samples left visible residue after detachment, SN-containing HCPEs showed no signs of leakage or staining (Supplementary Fig. 30b). No leakage was observed even under manually applied firm pressure (Fig. 4k). To further evaluate leakage under cyclic mechanical stress, the sample weight was monitored over repeated pressure cycles (Fig. 4l). A constant pressure of 25 kPa was applied repeatedly up to 1,000 cycles (Supplementary Fig. 32). Both polycationic (SN 0.6) and polyanionic (SN 0.9) HCPEs exhibited minimal mass change, whereas the ionogel control showed noticeable mass loss (Fig. 4m). These results confirm the stable integration of SN within the elastomer matrix.

Elastomeric properties and demonstrations of HCPEs

To verify that the incorporation of SN does not compromise the solid-state nature of the polymer films, we evaluated their viscoelastic properties using a rheometer. In both polycationic and polyanionic systems, the tanδ values remained below 1 across all SN loadings,

Fig. 4 | Electrical characteristics and stability of HCPEs. a–**c**, Electrical characteristics of polycationic elastomers. **d**–**f**, Electrical characteristics of polyanionic elastomers. **a**,**d**, Complex impedance spectra with various SN concentrations. Inset: magnified view for SN 0.4 and SN 0.6 in the range of 10^3–10^7 Hz (**a**). The solid lines represent fits to the equivalent circuit model shown in the inset of **d**. **b**,**e**, d.c. ionic conductivity, dissociated ion density and effective ion mobility at different SN ratios at 25 °C. **c**,**f**, Comparison of dissociated ion density by independent methods: electrochemical impedance spectroscopy (EIS) fitting and FTIR deconvolution. Data from **b**, **c**, **e** and **f** are presented as mean values ± standard deviation from three independent replicates. **g**, Comparison of $\sigma_{d.c.}$ and τ_C^{-1} of HCPEs to pristine and reported PEs. Insets: LED photographs at 1 MHz for pristine PEs and HCPEs. Scale bars, 1 cm. **h**, Normalized conductivity (σ/σ_0) of polycationic (SN 0.6) and polyanionic (SN 0.9) elastomers stored at 25 °C and 35% RH, where σ_0 denotes the initial conductivity. Inset: normalized weight (w/w_0) of polycationic (SN 0.6) and polyanionic (SN 0.9) elastomers stored at 25 °C and 90% RH, where w_0 denotes the initial weight. **i**,**j**, Water contact angles (WCA) for polycationic (**i**) and polyanionic (**j**) elastomers. Data are presented as mean values ± standard deviation from three independent replicates. **k**, Leakage test of HCPEs. (i) Polycationic (SN 0.6) and polyanionic (SN 0.9) elastomers were attached to oil paper. (ii) Firm pressure was manually applied. (iii) After detaching the samples, no visible leakage was observed. Scale bars, 1 cm. **l**, Schematic of the experimental setup for leakage test under cyclic pressure. The sample was placed on oil paper and compressed repeatedly. **m**, Normalized weight over the number of pressure cycles for polycationic (SN 0.6), polyanionic (SN 0.9) and a control ionogel composed of PVDF-HFP and [EMIM][TFSI]. The test was conducted using a maximum pressure of 25 kPa. CPE_{EDL}, constant phase element representing the non-ideal electric double-layer response.

https://doi.org/10.1038/s41563-026-02604-8

indicative of solid-like behaviour (Fig. 5a,b). This suggests that although T_g is reduced, the HCPEs behave as solid films (Fig. 5c). To evaluate the elastomeric nature of HCPEs under deformation, we conducted loading–unloading tests. Increasing the SN content in HCPEs improves elastic recovery with smaller hysteresis (Fig. 5d,e and Supplementary Figs. 33 and 34). Despite decreased fracture toughness due to lower energy dissipation (Fig. 5g), both HCPEs still exhibited low mechanical hysteresis over 1,000 cycles (Fig. 5f). As the addition of SN disrupts ion associations, the Young modulus decreased with increasing SN content (Fig. 5g and Supplementary Figs. 35–37).

Leveraging the enhanced ionic conduction, leakage-free behaviour and elasticity of HCPEs, we explored their application in capacitive pressure sensing. Unlike conventional capacitive sensors that rely on dielectric layers, electric double-layer (EDL)-based sensors use ionic conductors between metal electrodes[10,52]. Because the equivalent circuit of an ionic conductor is frequency dependent, effective EDL

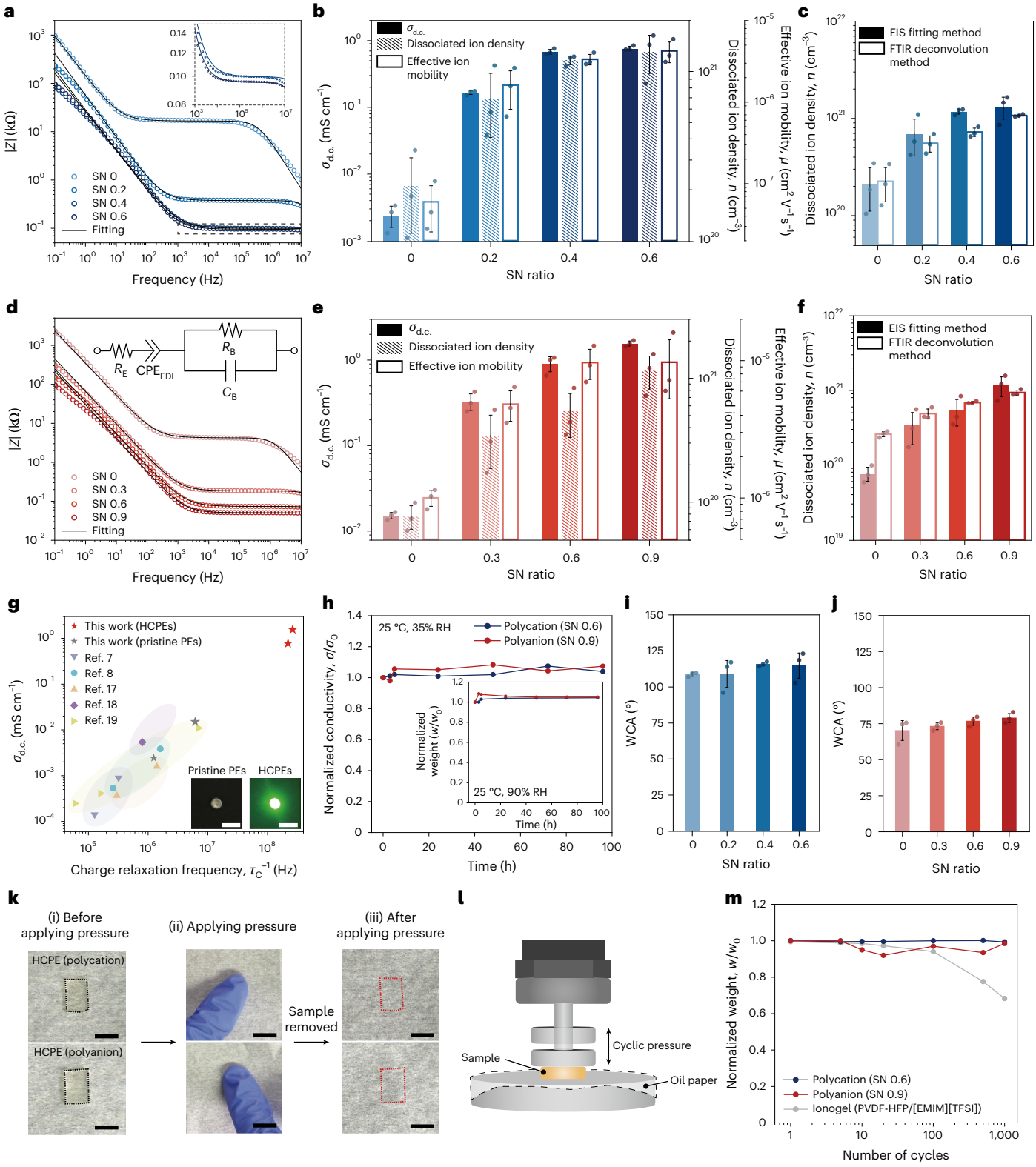

https://doi.org/10.1038/s41563-026-02604-8

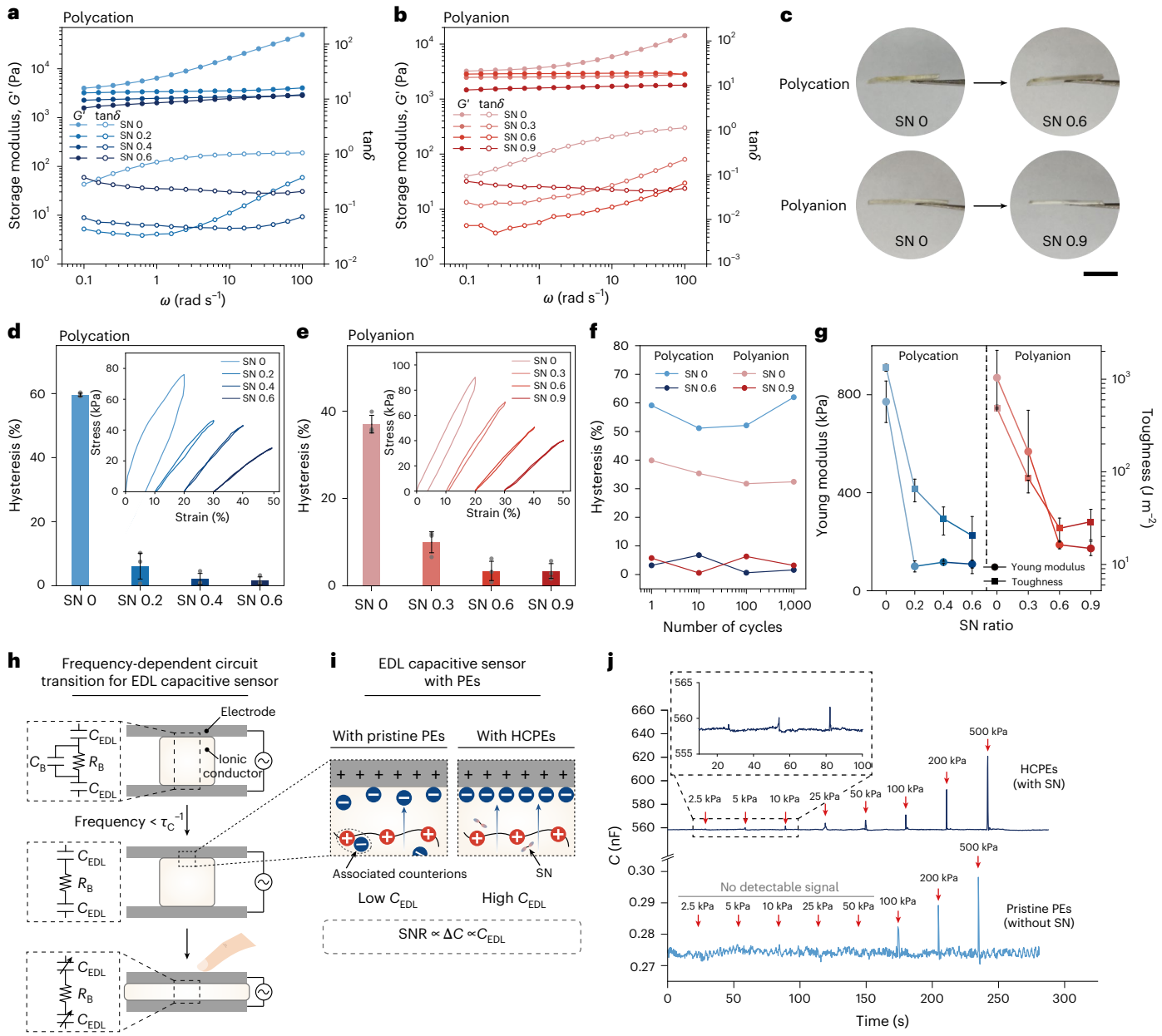

Fig. 5 | Elastomeric behaviour of HCPEs and its application as pressure sensors. **a**,**b**, Storage modulus (G', filled symbols) and loss factor (tanδ, open symbols) of polycationic (**a**) and polyanionic (**b**) elastomers, as a function of frequency with various SN concentrations. **c**, Photographs of polycationic (top) and polyanionic (bottom) elastomers with and without SN. Scale bar, 1 cm. **d**,**e**, Mechanical hysteresis of polycationic (**d**) and polyanionic (**e**) elastomers at different SN ratios. Insets: the stress–strain curves during loading–unloading, where 20% strain is applied for each sample. For visual clarity, curves for SN 0.2, SN 0.4 and SN 0.6 (**d**) and SN 0.3, SN 0.6 and SN 0.9 (**e**) are horizontally shifted by 10% intervals along the strain axis. Dots in **d** and **e** represent raw data ($n = 3$). **f**, Long-term mechanical hysteresis under 20% tensile strain over 1,000 loading–unloading cycles for polycationic and polyanionic elastomers, comparing samples with and without SN. **g**, Young modulus and toughness of polycationic and polyanionic elastomers with various SN concentrations. Data from **d**, **e** and **g** are presented as mean values ± standard deviation from three independent replicates. **h**, Schematic of EDL capacitive sensors. When the external a.c. field has a frequency below the τ_C^{-1}, the C_B becomes negligible, leaving C_{EDL} as the dominant capacitive component. When pressure is applied, the effective contact area increases, resulting in a change in C_{EDL}. **i**, Schematic of a comparison of EDL capacitive sensors using pristine PEs and HCPEs. At the electrode–electrolyte interface, HCPEs exhibit greater ionic accumulation due to enhanced ion dissociation and mobility, leading to a larger C_{EDL}. This results in an improved SNR. **j**, Capacitance of PEs with (top) and without (bottom) SN under a broad range of applied pressures. HCPEs show higher capacitance and enable sensing across a wide pressure range (2.5–500 kPa), indicating an enhanced SNR.

sensing requires the applied a.c. frequency to be lower than the charge relaxation frequency ($f_{a.c.} < \tau_C^{-1}$). In this regime, the bulk capacitance becomes negligible and the EDL capacitance dominates the capacitive response (Fig. 5h). When pressure is applied, the contact area between the electrode and ionic conductor increases, enabling pressure sensing[53]. The EDL capacitance (C_{EDL}) is proportional to the accumulation of ions at the interface between the electrode and the electrolyte. We, therefore, expected that our approach to increase n and μ would allow more ions to reach the interface more quickly, thereby increasing C_{EDL} (Fig. 5i). Since the signal-to-noise ratio (SNR) is determined by the magnitude of capacitance change (ΔC) under pressure, our strategy enables high signal output, as ΔC is proportional to C_{EDL} (Fig. 5i). Capaci-

https://doi.org/10.1038/s41563-026-02604-8

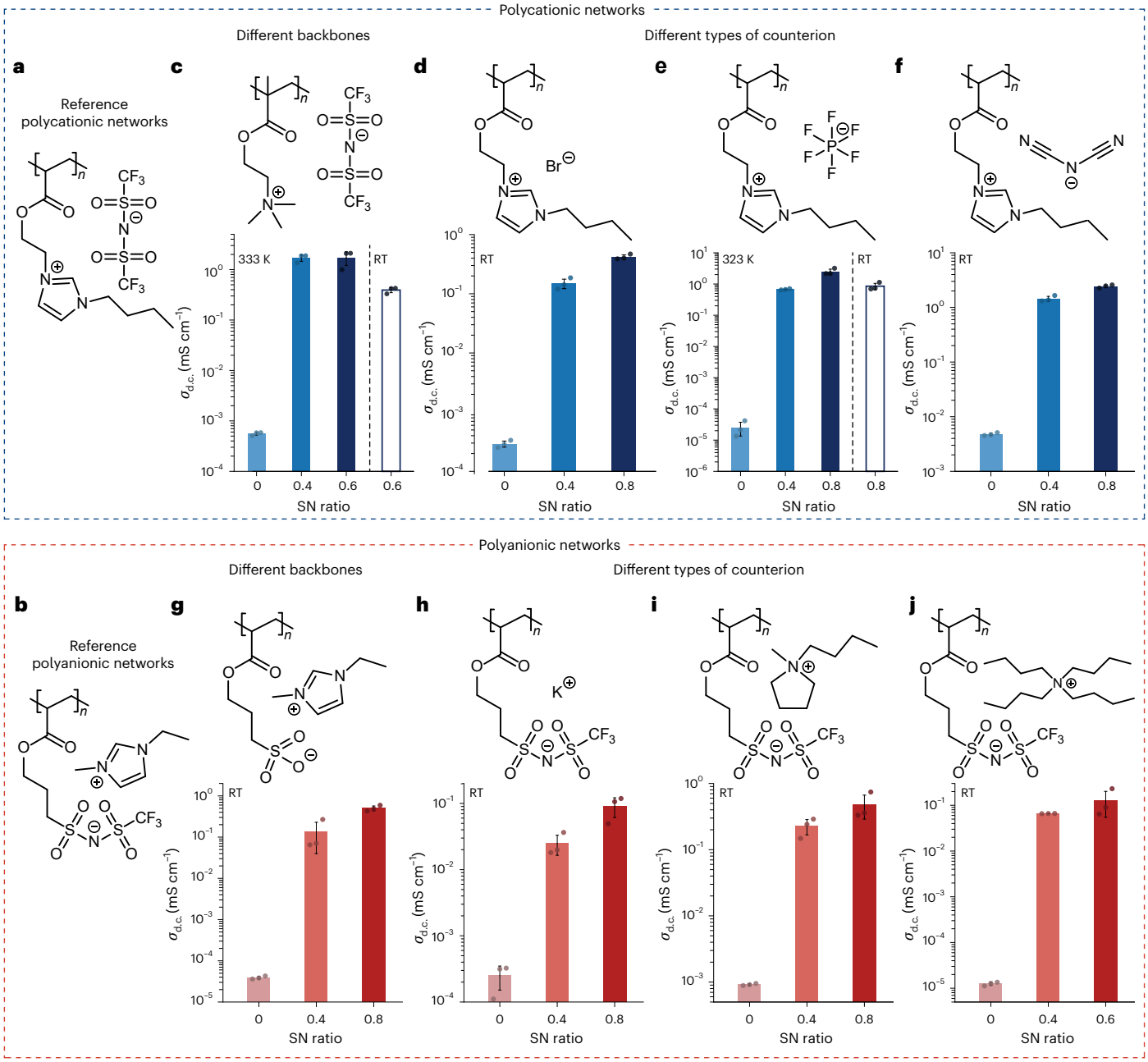

Fig. 6 | Versatile conductivity enhancement by a high-dielectric plasticizer in diverse single-ion-conducting polyelectrolyte networks. a,**b**, Chemical structures of the reference polycationic (**a**) and polyanionic (**b**) networks. RT, room temperature. **c**–**f**, d.c. ionic conductivity at different SN ratios for polycationic networks with different polymer backbones (**c**) and with different mobile counterions (**d**–**f**; bromide (**d**), hexafluorophosphate (**e**) and dicyanamide (**f**)), compared with the reference network in **a**. **g**–**j**, d.c. ionic conductivity at different SN ratios for polyanionic networks with different polymer backbones (**g**) and with different mobile counterions (**h**–**j**; potassium (**h**), 1-butyl-1-methylpyrrolidinium (**i**) and tetrabutylammonium (**j**)), compared with the reference network in **b**. Measurement temperatures are indicated in each panel. Filled bars show data measured at 333 K (**c**) or 323 K (**e**), and additional room-temperature data for SN 0.6 (**c**) and SN 0.8 (**e**) are shown as hollow bars separated by a dashed line. Data from **c**–**j** are presented as mean values ± standard deviation from three independent replicates.

tance measurements over time under varying pressures revealed that pristine PEs (without SN) could not distinguish capacitance changes from background noise below 100 kPa. By contrast, SN-containing HCPEs exhibited clear responses over a broad pressure range (2.5–500 kPa), indicating enhanced SNR (Fig. 5j, Supplementary Figs. 38 and 39 and Supplementary Table 6). To examine sensing performance under comparable mechanical deformation, we compared capacitance responses under the same compressive strain for PEs with and without SN. Only SN-containing HCPEs showed discernible capacitance changes, whereas pristine PEs remained at the noise level, indicating that the improved sensing performance is mainly governed by enhanced ionic conduction (Supplementary Fig. 40). These results demonstrate the potential of HCPEs as EDL capacitive sensors with enhanced signal clarity, enabled by improved ionic conduction and elasticity.

Versatile conductivity enhancement in diverse single-ion networks

To demonstrate the versatility of our high-dielectric plasticizer strategy, we applied SN to a series of chemically crosslinked single-

ion-conducting polyelectrolyte networks with different polymer backbones and counterions, spanning both polycationic and polyanionic systems (Fig. 6 and Supplementary Figs. 41–50). Specifically, we used 1-[2-acryloyloxyethyl]-3-butylimidazolium bis(trifluoromethane) sulfonimide (AT) (Fig. 6a) and 1-ethyl-3-methylimidazolium 3-[[[(trifluoromethyl)sulfonyl]amino]sulfonyl]propyl acrylate (EA) (Fig. 6b) as reference polycationic and polyanionic networks, respectively, and then varied either the polymer backbone (Fig. 6c,g) or the counterion species (Fig. 6d–f,h–j) and maintained the chemically crosslinked single-ion architecture. Across all networks, SN incorporation led to substantial conductivity enhancements, typically increasing $\sigma_{d.c.}$ from 10^{-5}–10^{-3} mS cm^{-1} to 0.1–2 mS cm^{-1} at the measured temperatures, corresponding to roughly 10^{2}–10^{5}-fold increases. For networks that are glassy at room temperature, the change in $\sigma_{d.c.}$ was evaluated at elevated temperatures (Fig. 6c,e). Nevertheless, after SN incorporation, these networks reached conductivities exceeding 0.1 mS cm^{-1} even at room temperature. Therefore, these results demonstrate that high-dielectric plasticization by SN provides an effective approach to boost ionic conductivity across diverse polyelectrolyte networks.

Discussion

In this study, we demonstrated HCPEs with leakage-free operation. The central design principle is to introduce a solid, electrically neutral, high-dielectric plasticizer that can be stably retained within polymer networks, thereby preserving the leakage-free and ion-selective nature of PEs and simultaneously promoting ion dissociation and ion mobility. Despite the single-ion constraint that allows only one ionic species to be mobile, the resulting conductivities approached those of liquid-based dual-ion conductors such as ionogels and ionic liquids. Consistently enhancing conductivity across chemically distinct networks, this strategy expands the application scope of solid-state single-ion conductors that have been constrained by their intrinsically low conductivity. Considering that the limitations of ionic transport stem from both strong ion pairing and limited segmental dynamics, it would be valuable to design high-dielectric plasticizers with tailored molecular architectures for a range of solid-state ionic conductors. We anticipate that the strategy demonstrated here will contribute broadly to the development of next-generation solid-state ionic devices requiring fast, stable and selective ion transport such as wearable energy storage devices, ionic thermoelectric devices, ionic diodes and flexible electrochemical systems.

Online content

Any methods, additional references, Nature Portfolio reporting summaries, source data, extended data, supplementary information, acknowledgements, peer review information; details of author contributions and competing interests; and statements of data and code availability are available at https://doi.org/10.1038/s41563-026-02604-8.

References

1. Maffeo, C., Bhattacharya, S., Yoo, J., Wells, D. & Aksimentiev, A. Modeling and simulation of ion channels. *Chem. Rev.* **112**, 6250–6284 (2012).
2. Xiao, K., Wan, C., Jiang, L., Chen, X. & Antonietti, M. Bioinspired ionic sensory systems: the successor of electronics. *Adv. Mater.* **32**, 2000218 (2020).
3. Han, S. et al. Sequencing polymers to enable solid-state lithium batteries. *Nat. Mater.* **22**, 1515–1522 (2023).
4. Rivnay, J. et al. Organic electrochemical transistors. *Nat. Rev. Mater.* **3**, 17086 (2018).
5. Na, H. et al. Hydrogel-based strong and fast actuators by electroosmotic turgor pressure. *Science* **376**, 301–307 (2022).
6. Boahen, E. K. et al. Ultrafast, autonomous self-healable iontronic skin exhibiting piezo-ionic dynamics. *Nat. Commun.* **13**, 7699 (2022).
7. Kim, H. J., Chen, B., Suo, Z. & Hayward, R. C. Ionoelastomer junctions between polymer networks of fixed anions and cations. *Science* **367**, 773–776 (2020).
8. Lee, S. W. et al. Intrinsically stretchable ionoelastomer junction logic gate synchronously deformable with liquid metal. *Appl. Phys. Rev.* **9**, 041404 (2022).
9. Kim, C.-C., Lee, H.-H., Oh, K. H. & Sun, J.-Y. Highly stretchable, transparent ionic touch panel. *Science* **353**, 682–687 (2016).
10. He, X. et al. Highly conductive and stretchable nanostructured ionogels for 3D printing capacitive sensors with superior performance. *Nat. Commun.* **15**, 6431 (2024).
11. Lee, H. R., Kim, C. C. & Sun, J. Y. Stretchable ionics—a promising candidate for upcoming wearable devices. *Adv. Mater.* **30**, 1704403 (2018).
12. Kim, S. et al. Side-chain engineered p or n-type nonaqueous polymeric ionic gels for sustainable ionic thermoelectrics. *Adv. Funct. Mater.* **33**, 2305499 (2023).
13. Sun, S., Li, M., Shi, X. L. & Chen, Z. G. Advances in ionic thermoelectrics: from materials to devices. *Adv. Energy Mater.* **13**, 2203692 (2023).
14. Lee, H. R. et al. A stretchable ionic diode from copolyelectrolyte hydrogels with methacrylated polysaccharides. *Adv. Funct. Mater.* **29**, 1806909 (2019).
15. Schroeder, T. B. et al. An electric-eel-inspired soft power source from stacked hydrogels. *Nature* **552**, 214–218 (2017).
16. Park, J.-M., Lim, S. & Sun, J.-Y. Materials development in stretchable iontronics. *Soft Matter* **18**, 6487–6510 (2022).
17. Shin, H., Shin, J., Hayward, R. C. & Kim, H. J. Ionoelastomers at electrified interfaces: differential electric double-layer capacitances of cross-linked polymeric ions and mobile counterions. *Macromolecules* **56**, 7827–7836 (2023).
18. Ming, X. et al. Highly transparent, stretchable, and conducting ionoelastomers based on poly(ionic liquid)s. *ACS Appl. Mater. Interfaces* **13**, 31102–31110 (2021).
19. He, Y., Cheng, Y., Yang, C. & Guo, C. F. Creep-free polyelectrolyte elastomer for drift-free iontronic sensing. *Nat. Mater.* **23**, 1107–1114 (2024).
20. Park, J. et al. Elastomeric polymer network electrolyte: synthesis, properties, and applications. *Prog. Polym. Sci.* **163**, 101944 (2025).
21. Bocharova, V. & Sokolov, A. P. Perspectives for polymer electrolytes: a view from fundamentals of ionic conductivity. *Macromolecules* **53**, 4141–4157 (2020).
22. Choi, S.-G., Kang, S.-H., Lee, J.-Y., Park, J.-H. & Kang, S.-K. Recent advances in wearable iontronic sensors for healthcare applications. *Front. Bioeng. Biotechnol.* **11**, 1335188 (2023).
23. Lee, O. A., McBride, M. K., Ticknor, M., Sharpes, J. & Hayward, R. C. Pendent sulfonylimide ionic liquid monomers and ionoelastomers via SuFEx click chemistry. *Chem. Mater.* **35**, 10030–10040 (2023).
24. Chen, Y. et al. Helical peptide structure improves conductivity and stability of solid electrolytes. *Nat. Mater.* **23**, 1539–1546 (2024).
25. Juger, J. et al. Polymeric ionic liquid based interpenetrating polymer network for all-solid self-standing polyelectrolyte material. *Eur. Polym. J.* **106**, 257–265 (2018).
26. O'Harra, K. E., Timmermann, G. M., Bara, J. E. & Miller, K. M. Designing ionic liquid-derived polymer composites from poly (ionic liquid)–ionene semi-interpenetrating networks. *ACS Applied Polymer Materials* **3**, 1995–2004 (2021).
27. Li, C. et al. Polyelectrolyte elastomer-based ionotronic sensors with multi-mode sensing capabilities via multi-material 3D printing. *Nat. Commun.* **14**, 4853 (2023).
28. Wang, P. et al. Single-ion gel polymer electrolyte based on in-situ UV irradiation cross-linked polyimide complexed with PEO for lithium-ion batteries. *Macromol. Rapid Commun.* **44**, 2200865 (2023).

29. Alarco, P.-J., Abu-Lebdeh, Y., Abouimrane, A. & Armand, M. The plastic-crystalline phase of succinonitrile as a universal matrix for solid-state ionic conductors. *Nat. Mater.* **3**, 476–481 (2004).
30. Ma, B., Nguyen, T. D. & Olvera de la Cruz, M. Control of ionic mobility via charge size asymmetry in random ionomers. *Nano Lett.* **20**, 43–49 (2019).
31. Xu, H. et al. Shielding the electrostatic attraction by design of zwitterionic single ion conducting polymer electrolyte with high dielectric constant. *J. Membr. Sci.* **651**, 120452 (2022).
32. Bruce, P. G. *Solid State Electrochemistry* (Cambridge Univ. Press, 1997).
33. Voigt, N. & van Wüllen, L. The effect of plastic-crystalline succinonitrile on the electrolyte system PEO:$LiBF_4$: insights from solid state NMR. *Solid State Ionics* **260**, 65–75 (2014).
34. Wohlfarth, C. in *CRC Handbook of Chemistry and Physics* 6 (CRC Press, 1994).
35. Sengwa, R. J., Kaur, K. & Chaudhary, R. Dielectric properties of low molecular weight poly(ethylene glycol)s. *Polym. Int.* **49**, 599–608 (2000).
36. Kiefer, J., Fries, J. & Leipertz, A. Experimental vibrational study of imidazolium-based ionic liquids: Raman and infrared spectra of 1-ethyl-3-methylimidazolium bis(trifluoromethylsulfonyl)imide and 1-ethyl-3-methylimidazolium ethylsulfate. *Appl. Spectrosc.* **61**, 1306–1311 (2007).
37. Kong, Z. et al. Ultrafast underwater self-healing piezo-ionic elastomer via dynamic hydrophobic-hydrolytic domains. *Nat. Commun.* **15**, 2129 (2024).
38. Kweon, H. et al. Ion trap and release dynamics enables nonintrusive tactile augmentation in monolithic sensory neuron. *Sci. Adv.* **9**, eadi3827 (2023).
39. Zhao, W. et al. Exceptional n-type thermoelectric ionogels enabled by metal coordination and ion-selective association. *Sci. Adv.* **9**, eadk2098 (2023).
40. Dhumal, N. R., Noack, K., Kiefer, J. & Kim, H. J. Molecular structure and interactions in the ionic liquid 1-ethyl-3-methylimidazolium bis (trifluoromethylsulfonyl) imide. *J. Phys. Chem. A* **118**, 2547–2557 (2014).
41. Sengwa, R. & Dhatarwal, P. Predominantly chain segmental relaxation dependent ionic conductivity of multiphase semicrystalline PVDF/PEO/$LiClO_4$ solid polymer electrolytes. *Electrochim. Acta* **338**, 135890 (2020).
42. Yun, S., Hwang, I., Choi, J. W. & Kim, S. Y. Enhanced ionic conductivity via suppressed crystallization and strengthened dynamics in solid polymer-blend electrolytes: a comprehensive broadband dielectric spectroscopy study. *Macromolecules* **58**, 639–651 (2024).
43. Bandara, T. M. W. J. & Mellander, B. E. in *Ionic Liquids: Theory, Properties, New Approaches* 383–406 (2011).
44. Arof, A., Amirudin, S., Yusof, S. & Noor, I. A method based on impedance spectroscopy to determine transport properties of polymer electrolytes. *Phys. Chem. Chem. Phys.* **16**, 1856–1867 (2014).
45. Winie, T., Arof, A. K. & Thomas, S. *Polymer Electrolytes: Characterization Techniques and Energy Applications* (John Wiley & Sons, 2019).
46. Park, C. S., Park, J., Lee, H. & Sun, J.-Y. Phase-transitional ionic thermocells for the enhanced thermoelectric efficiency. *ACS Appl. Mater. Interfaces* **17**, 32423–32431 (2025).
47. Jamal, A., Muhammad, F., Ali, A. & Winie, T. Blends of hexanoyl chitosan/epoxidized natural rubber doped with EMImTFSI. *Ionics* **23**, 357–366 (2017).
48. Yap, A. Y., Phang, S. W. & Liew, C.-W. Synthesis of poly(vinyl acetate)-based gel polymer electrolyte for application in electric double layer capacitors. *Ionics* **29**, 3317–3334 (2023).
49. Singh, P., Bharati, D. C., Kumar, H. & Saroj, A. Ion transport mechanism and dielectric relaxation behavior of PVA-imidazolium ionic liquid-based polymer electrolytes. *Phys. Scr.* **94**, 105801 (2019).
50. Choi, U. H. et al. Ionic conduction and dielectric response of poly(imidazolium acrylate) ionomers. *Macromolecules* **45**, 3974–3985 (2012).
51. Klein, R. J. et al. Modeling electrode polarization in dielectric spectroscopy: ion mobility and mobile ion concentration of single-ion polymer electrolytes. *J. Chem. Phys.* **124**, 144903 (2006).
52. You, I. et al. Artificial multimodal receptors based on ion relaxation dynamics. *Science* **370**, 961–965 (2020).
53. Chang, Y. et al. First decade of interfacial iontronic sensing: from droplet sensors to artificial skins. *Adv. Mater.* **33**, 2003464 (2021).

Methods

Materials

1-Butylimidazole, poly(ethylene glycol) diacrylate (PEGDA; average M_n, 250), 3-sulfopropyl acrylate potassium salt, potassium hydrogenfluoride, SN, triethylene glycol monomethyl ether, imidazole, silver nitrate, 2-(methacryloyloxy)ethyl trimethylammonium chloride, potassium hexafluorophosphate, 1-butyl-1-methylpyrrolidinium chloride, tetrabutylammonium chloride, dimethyl sulfoxide-d_6, deuterated chloroform and DMC were purchased from Sigma-Aldrich. 2-Bromoethyl acrylate (stabilized with 900–1,500 ppm of 4-methoxyphenol), oxalyl chloride, potassium carbonate and 1-ethyl-3-methylimidazolium chloride were purchased from Alfa Aesar. Trifluoromethanesulfonamide, lithium bis(trifluoromethane) sulfonimide, 2,2-dimethoxy-2-phenylacetophenone (DMPA), PEG 200, *p*-toluenesulfonyl chloride, sodium dicyanamide and 1,4-butanesultone were purchased from TCI Chemicals. *N*,*N*-Dimethylformamide (DMF; 99.8%), DCM (>99.8%), tetrahydrofuran (99.8%), acetonitrile (MeCN; 99.8%), ethyl acetate (99.8%) and sodium hydroxide were purchased from Daejung Industry. All chemicals were used as received, whereas DMF was used after being dried over 4-Å molecular sieves.

Preparation of pristine PEs

The monomers for AT and EA were synthesized following previous work[7,17] (Supplementary Methods and Supplementary Figs. 1 and 2). PEGDA (2 mol%) was mixed with AT and EA monomer. Next, 0.5 mol% of DMPA solution in ethanol (100 mg ml^{-1}) was added as a photoinitiator. After mixing, ethanol was removed under a vacuum of <10^{-1} torr at room temperature. The viscous AT (or EA) mixture was then injected into a polytetrafluoroethylene mould separated by 400-µm-thick poly(ethylene terephthalate) spacers. Free radical polymerization was initiated by exposure to 365-nm ultraviolet light for 30 min. After polymerization, the residual monomers were washed out by soaking the PEs in DCM overnight. Finally, the PEs were dried at 60 °C in a vacuum oven to completely remove residual solvents.

Preparation of HCPEs

To fabricate HCPEs, the as-prepared PEs (polycation or polyanion) were first weighed to determine the required amount of SN. SN was dissolved in DCM at a weight ratio of 1:1.2 (SN:DCM) to prepare a homogeneous casting solution. The SN/DCM solution was then uniformly applied onto the PEs. The samples were sealed in a Petri dish and incubated at 40 °C for 12 h to allow the thorough diffusion of SN into the elastomer network. The resulting elastomers were optically transparent without signs of phase separation or crystallized SN domains. To remove the residual solvent, the samples were subsequently placed under a vacuum of <10^{-1} torr at 40 °C for an additional 2 h.

Preparation of PEs with other additives

To prepare PEs containing alternative additives, the as-prepared PEs (polycation or polyanion) were first weighed to determine the appropriate additive loading. A suitable amount of PEG 200 or DMC was dissolved in DCM to form a homogeneous solution, which was then uniformly applied onto the PEs. The samples were sealed and incubated at 40 °C for 12 h to allow additive diffusion into the elastomer network. Residual DCM was subsequently removed by drying the samples under vacuum (<10^{-1} torr) at 40 °C for an additional 2 h. For the ZIL, a high-dielectric additive, the synthesis scheme and dielectric property are provided in Supplementary Fig. 10. A suitable amount of ZIL was dissolved in MeCN and uniformly applied onto the PEs. The samples were placed at 40 °C for 12 h to promote diffusion, followed by vacuum drying at 60 °C for 4 h to remove residual MeCN.

Preparation of various polyelectrolyte networks

Various polyelectrolyte networks were prepared using ionic monomers synthesized according to the procedures described in the Supplementary Methods and characterized by NMR spectroscopy (Supplementary Figs. 41–48). For all monomers except potassium 3-[[[(trifluoromethyl)sulfonyl]amino]sulfonyl]propyl acrylate, the polymerization and washing steps were identical to those used for the pristine AT and EA PEs.

For potassium 3-[[[(trifluoromethyl)sulfonyl]amino]sulfonyl]propyl acrylate, the solid monomer was first dissolved in DMF at a mass ratio of 1:0.6 (monomer:DMF) with stirring to obtain a viscous solution. PEGDA (2 mol%) and DMPA (0.5 mol%) were then added and stirred thoroughly. The resulting precursor mixture was degassed for 10 min. The viscous mixture was injected into a polytetrafluoroethylene mould separated by 400-µm-thick poly(ethylene terephthalate) spacers. Free radical polymerization was initiated by exposure to 365-nm ultraviolet light for 4 h. After polymerization, the residual monomers were washed out by soaking the obtained polyelectrolyte networks in MeCN overnight. Finally, the networks were dried at 60 °C in a vacuum oven for 24 h to completely remove residual solvents.

Preparation of highly conductive polyelectrolyte networks

To prepare highly conductive polyelectrolyte networks, SN was introduced into the as-prepared polyelectrolyte networks using the same solvent-swelling method as described for HCPEs.

For the networks prepared from potassium 3-[[[(trifluoromethyl)sulfonyl]amino]sulfonyl]propyl acrylate and 1-[2-acryloyloxyethyl]-3-butylimidazolium bromide, SN was introduced in an analogous manner, except that MeCN was used instead of DCM. The samples were placed at 40 °C for 12 h to promote diffusion, followed by vacuum drying at 60 °C for 4 h to remove residual MeCN.

Preparation of PVDF-HFP/[EMIM][TFSI] ionogel

PVDF-HFP (8 g) was dissolved in acetone (72 ml) under stirring for 30 min at room temperature. [EMIM][TFSI] (8 g) was then added and the mixture was stirred for a further 10 min at room temperature to obtain a homogeneous precursor solution. The resulting solution was cast onto a glass Petri dish, and left at room temperature for 24 h to allow the evaporation of acetone. The dried film was subsequently transferred to a vacuum oven and dried at 40 °C for 1 h to remove the residual solvent, yielding the PVDF-HFP/[EMIM][TFSI] ionogel.

NMR, FTIR and Raman characterizations

The ^{1}H and ^{19}F NMR spectra were collected on a 400-MHz NMR spectrometer (AVANCE NEO 400, Bruker) at the National Instrumentation Center for Environmental Management, Seoul National University. For SN-containing samples, SN was directly dissolved into the synthesized monomer and stirred for 15 min to form a homogeneous solution. Approximately 20 mg of the resulting solution was then dissolved in deuterated chloroform for NMR analysis. The synthesized monomers were dissolved in dimethyl sulfoxide-d_6 and characterized using a 600-MHz NMR spectrometer (AVANCE III HD, Bruker).

An FTIR spectrometer (Nicolet iS50, Thermo Fisher Scientific) was used to conduct the FTIR spectroscopic analysis. All data were measured in the ATR mode. Peak shifts in HCPEs were confirmed by the FTIR spectra.

Raman spectra were acquired using a LabRAM HR Evolution Raman spectrometer (HORIBA) equipped with a 633-nm laser at the Research Institute of Advanced Materials, Seoul National University. The laser power was set to 50%. For point measurements, the spectra were collected with an acquisition time of 100 s and one accumulation. Raman mapping was performed under identical laser conditions (633 nm, 50% power) with an acquisition time of 10 s and one accumulation per point. A spectral range of 2,200–2,500 cm^{-1} was scanned over a 10 × 10 grid with a step size of 3.3 µm.

Electrical characterizations

Impedance and dielectric measurements were conducted using a Novocontrol Concept 40 dielectric spectrometer equipped with a

Quatro Cryosystem temperature control unit. Measurements were performed over a frequency range of 10^{-1} to 10^{7} Hz with an applied a.c. voltage of 40 mV (root mean square (r.m.s.)). Samples were sandwiched between a pair of disposable gold-plated electrodes (BDS 1301) with a fixed sample diameter of 9 mm and placed in the ZGS sample cell. To ensure measurement reliability, all measurements were carried out in a temperature-controlled chamber at 25 °C. The complex impedance data were transformed into complex conductivity, with the real part of conductivity ($\sigma'(\omega)$) calculated as

$$\sigma'(\omega) = \frac{l}{A} \times \frac{Z'(\omega)}{Z'(\omega)^2 + Z''(\omega)^2},$$

where l is the sample thickness; A is the electrode area; and $Z'(\omega)$ and $Z''(\omega)$ are the real and imaginary components of impedance, respectively. The frequency-independent plateau region of $\sigma'(\omega)$ was identified as the d.c. conductivity ($\sigma_{d.c.}$). Additionally, the plateau conductivity obtained from high-frequency random barrier model fitting was taken as $\sigma_{d.c.}$ (Supplementary Fig. 19). The d.c. conductivity was also independently calculated from the bulk resistance (R_B) extracted from Nyquist plots using the relation $\sigma = l/AR_B$.

Temperature-dependent conductivity measurements were performed from 0 to 70 °C in 10-K increments, with a stabilization time of 15 min at each temperature. Measurements were performed over a frequency range of 10^{0}–10^{7} Hz with an applied a.c. voltage of 40 mV (r.m.s.). To confirm the Arrhenius-to-VTF crossover, the polycation elastomer (SN 0) was further examined over an extended range from −60 to 50 °C in 10-K intervals, with a stabilization time of 15 min at each temperature. Measurements were performed over a frequency range of 10^{-1} to 10^{7} Hz with the same bias. Below the glass transition temperature, the conductivity followed the Arrhenius relation

$$\sigma(T) = \sigma_0 \exp\left[-\frac{E_a}{RT}\right],$$

where E_a is the activation energy and R is the gas constant. Above T_g, the conductivity followed the VTF relation[3]

$$\sigma(T) = AT^{-0.5} \exp\left[-\frac{B}{R(T - T_0)}\right],$$

where A is a pre-exponential factor, B is the pseudo-activation energy and T_0 is the Vogel temperature.

For environmental stability tests under ambient and 90% RH, d.c. conductivity was measured using a precision LCR meter (E4980A, Agilent Technologies), over a frequency range of 20–10^{6} Hz with an applied a.c. voltage of 40 mV (r.m.s.). The calculation method for d.c. conductivity was consistent with that described above.

Jonscher's power law ($\sigma(\omega) = \sigma_{d.c.}[1 + (\omega/\omega_p)^n]$, where n is the power-law exponent ($0 < n < 1$) and ω_p is ion hopping frequency) was used to construct a master curve of HCPEs' conductivity across different SN compositions. Scaling of the frequency-dependent a.c. conductivity is

$$\frac{\sigma}{\sigma_{d.c.}} = F\left(\frac{\omega}{\omega_p}\right),$$

where F is a scaling function independent of concentration and temperature.

Mechanical characterization

All mechanical tests were performed using a universal testing machine (Instron 3343) equipped with a 50-N load cell. Elastomer samples were cut into rectangular shapes and adhered to acrylic-sheet-based grippers using Krazy glue (Supplementary Fig. 35). The gauge length between grippers was fixed at 5 mm. The stretch rate was maintained at a constant rate of 4 min^{-1} throughout the tests. The Young modulus was determined from the initial slope of the stress–strain curves. Tensile loading–unloading tests were performed using the same setup, under an applied strain of 20%. For fracture toughness measurements, a notch with a length equal to half of the sample width was introduced before testing. Additional measurements were conducted at various strain rates to investigate mechanical hysteresis. Unless otherwise noted, the strain rate was set to 0.1 s^{-1}. Hysteresis was quantified following a previously reported method[54].

The viscoelastic properties of the PEs were investigated using a rheometer (DHR-2, TA Instruments). Samples were cut into circular discs with a diameter of 10 mm and a thickness of 500 µm. A parallel-plate geometry was used, and the applied normal preload was set to 0.3 N. Frequency sweep tests were conducted over an angular frequency range of 100 to 0.1 rad s^{-1} under a constant shear strain of 3%. Storage modulus (G'), loss modulus (G'') and loss factor ($\tan\delta$) were measured as a function of angular frequency.

Contact angle measurement

A contact angle analyser (FEMTOFAB, SmartDrop) was used to measure the contact angle. A 4-µl droplet of deionized water was placed on the sample surface at room temperature, and the contact angle was measured 30 s after water deposition. To evaluate wettability on commercial oil paper using liquid SN and PEG 200, a Peltier device was placed beneath the oil paper and maintained at 60 °C. Each liquid was preheated at 60°C for 30 min, after which a 4-µl droplet was placed onto the oil paper surface. The contact angle was measured 30 s after droplet deposition.

Device demonstration system

For device demonstration, pristine PEs and HCPEs were prepared. Each sample was fabricated into a disc shape with a diameter of 9 mm and a thickness of 400 µm. A metal–insulator–metal (MIM) structure was assembled by placing each sample between two gold electrodes.

The assembled MIM devices were then integrated into a circuit containing a waveform generator (Agilent 33600A series) and a commercial LED. An a.c. signal with a peak-to-peak voltage of 6 V was applied to the devices and the LED threshold voltage (V_{th}) was 2 V. The LED response was monitored to evaluate the ionic conduction behaviour of the elastomers.

For pressure-sensing applications, MIM devices were mounted on a universal testing machine (Instron 3343) equipped with a 1-kN load cell, and compressed under defined pressures. The capacitance of the sensor was measured using a precision LCR meter (E4980A, Agilent Technologies). For strain-controlled measurements, samples with identical geometry were prepared and assembled into MIM devices, which were then compressed to a fixed compressive strain of 10%.

Data availability

Source data are provided with this paper. Additional data supporting the findings of this study are included in the Supplementary Information.

References

54. Cho, Y. E., Lee, S., Ma, S. J. & Sun, J.-Y. Network design for soft materials: addressing elasticity and fracture resistance challenges. *Soft Matter* **21**, 1603–1623 (2025).

Acknowledgements

This research was supported by National Research Foundation of Korea (NRF) grants funded by the Korean Government (grant numbers RS-2022-NR067540 and RS-2024-00459269 to J.-Y.S.). The Institute of Engineering Research at Seoul National University provided research facilities for this work.

Author contributions

S.M., S.A. and J.-M.P. conceived the idea. S.M. developed the materials and methods. S.M. and S.A. conducted the NMR and rheological

measurements. S.M., S.A. and J.-M.P. interpreted the results. S.M., S.-Y.C. and Y.E.C. designed the schematics and S.M., H.L. and S.W.M. conducted the photographic documentation of the experiments. S.-W.L., D.-y.L., M.K., Y.H.L. and Y.-W.K. provided advice on revising the main paper. S.M., T.-W.L. and J.-Y.S. analysed the results. S.M. and J.-Y.S. wrote the paper. J.-Y.S. supervised the study.

Competing interests
The authors declare no competing interests.

Additional information
Extended data is available for this paper at https://doi.org/10.1038/s41563-026-02604-8.

Supplementary information The online version contains supplementary material available at https://doi.org/10.1038/s41563-026-02604-8.

Correspondence and requests for materials should be addressed to Jeong-Yun Sun.

Peer review information *Nature Materials* thanks Costantino Creton, Canhui Yang and the other, anonymous, reviewer(s) for their contribution to the peer review of this work.

https://doi.org/10.1038/s41563-026-02604-8

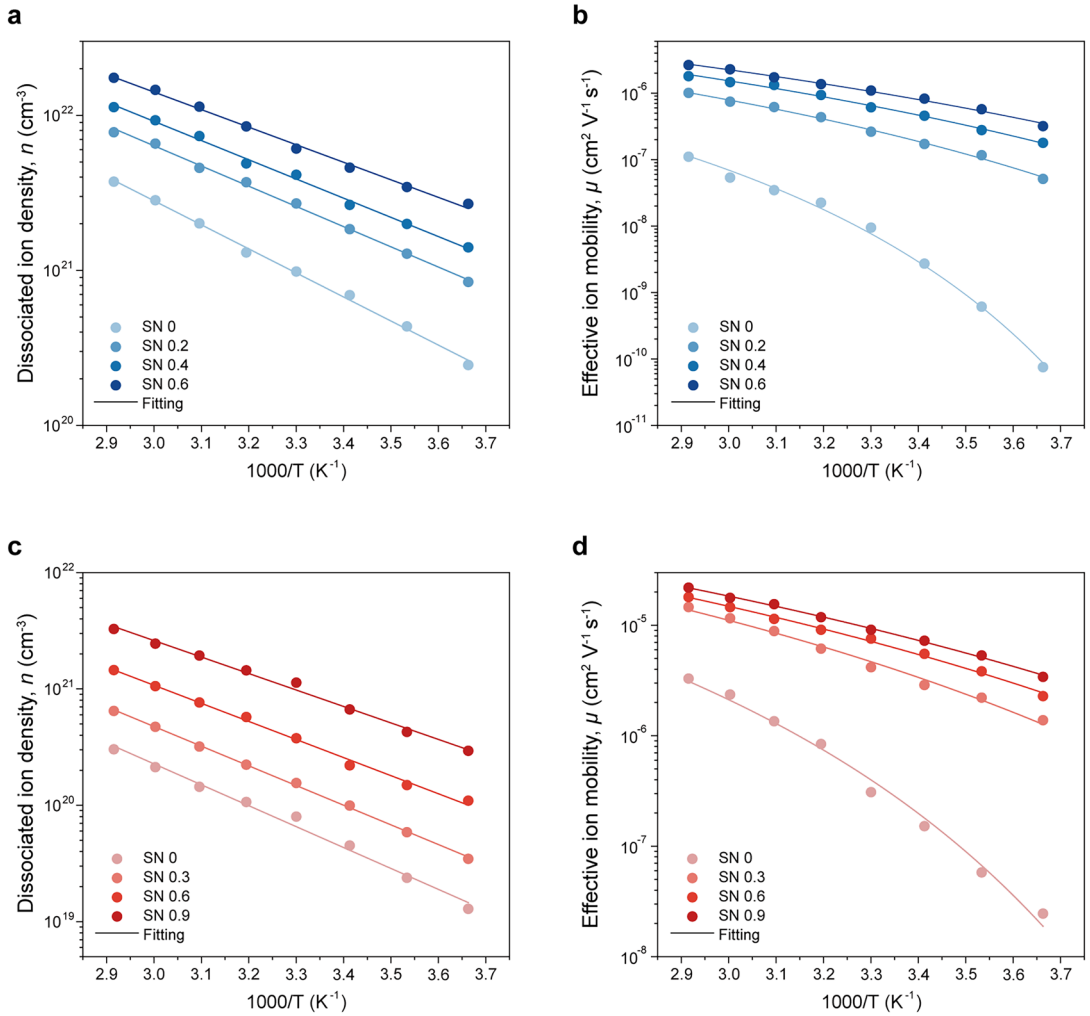

Extended Data Fig. 1 | Temperature dependence of dissociated ion density and effective ion mobility. a,b, Temperature dependence of dissociated ion density **(a)** and effective ion mobility **(b)** of polycationic elastomers. **c,d**, Temperature dependence of dissociated ion density **(c)** and effective ion mobility **(d)** of polyanionic elastomers. The dissociated ion density follows an Arrhenius relation, whereas the effective ion mobility follows a Vogel–Tammann–Fulcher (VTF) relation.

https://doi.org/10.1038/s41563-026-02604-8

Extended Data Table 1 | The value of ion density by FTIR deconvolution method

Polymer	+ Additive	Associated ions (%)	Dissociated ions (%)	Dissociated ion density ($\times 10^{20}$ cm^{-3})
Polycation (AT)	Pristine	91.28	8.72	2.24
Polycation (AT)	+ SN 0.2	77.10	22.90	5.51
Polycation (AT)	+ SN 0.4	66.35	33.65	7.19
Polycation (AT)	+ SN 0.6	48.09	51.91	10.63
Polyanion (EA)	Pristine	88.89	11.11	2.59
Polyanion (EA)	+ SN 0.3	77.94	22.06	4.89
Polyanion (EA)	+ SN 0.6	62.15	37.85	6.89
Polyanion (EA)	+ SN 0.9	45.04	54.96	9.34

All values are presented as mean values from three independent samples. The total ion concentration was calculated by dividing the molar amount of ions by the sample volume and converting it to number density using Avogadro's number.